



Article

# Performance Evaluation of Cross-Correlation Based Photoacoustic Measurement of a Single Object with Sinusoidal Linear Motion

Kotaro Fujinami  and Katsuaki Shirai \* 

Department of Mechanical Engineering, Shibaura Institute of Technology, 3 Chome-7-5 Toyosu, Koto City, Tokyo 135-8548, Japan; md22089@shibaura-it.ac.jp

\* Correspondence: kshirai@shibaura-it.ac.jp

**Abstract:** Photoacoustic (PA) velocimetry holds the advantage of detecting ultrasound signals from selective targets sensitive to specific wavelengths of light irradiation. In particular, it is expected to be applied for measuring blood flow in microvasculature. However, PA velocimetry has not been sufficiently investigated for small velocity ranges down to several tens of millimeters per second. This study evaluates the performance and uncertainty of PA velocity measurements using a single graphite cylinder (GC) as a moving object. A pair of short laser pulses irradiated the object within a brief time interval. The velocity was measured based on the cross-correlation peak of successive PA signal pairs in the time domain. The limiting measurement uncertainty was 3.4 mm/s, determined by the sampling rate of the digitizer. The object motion was controlled in a sinusoidal linear motion, realized using a loudspeaker. With the PA measurement, the velocity of the object was obtained with a time resolution in milliseconds and with directional discrimination. Notably, the PA velocity measurements successfully provided the local velocities of the object across a wide range, with the reference velocity obtained as the time derivative of the displacement data acquired using a laser displacement sensor (LDS). The PA measurement exhibited uncertainties ranging from 0.86 to 2.1 mm/s for the maximum and minimum velocities during the experiment. The uncertainties are consistent with those in stationary cases, and nearly constant in the investigated velocity range. Furthermore, the PA measurements revealed local fine velocities of the object, which were not resolved by the reference velocities of the LDS measurements. The capability of the PA velocity measurement was found to be advantageous for measurements of objects with dynamic variations in magnitude and direction.

**Keywords:** photoacoustic; ultrasound; velocity measurement; cross-correlation; pulsed laser; sinusoidal motion; measurement uncertainty; phase-resolved measurement



**Citation:** Fujinami, K.; Shirai, K. Performance Evaluation of Cross-Correlation Based Photoacoustic Measurement of a Single Object with Sinusoidal Linear Motion. *Appl. Sci.* **2023**, *13*, 13202. <https://doi.org/10.3390/app132413202>

Academic Editor: Vladislav Toronov

Received: 31 July 2023

Revised: 5 December 2023

Accepted: 8 December 2023

Published: 12 December 2023



**Copyright:** © 2023 by the authors. Licensee MDPI, Basel, Switzerland. This article is an open access article distributed under the terms and conditions of the Creative Commons Attribution (CC BY) license (<https://creativecommons.org/licenses/by/4.0/>).

## 1. Introduction

The photoacoustic (PA) effect refers to the generation of ultrasound waves when a light absorbing material absorbs energy from light irradiated at a specific wavelength and undergoes volumetric expansion. This phenomena involves a conversion mechanism where heat energy is directly coupled to vibrational modes [1,2]. This thermoelastic process is governed by thermal expansion, in which a pressure build-up is generated, releasing a stress wave. Thermoelastic mechanisms can efficiently convert the absorbed energy into acoustic pressure waves, particularly when the period of optical excitation is short. The resulting ultrasound pressure waves are known as PA waves [3].

The applications of the PA effect encompass in vivo three-dimensional visualization using PA imaging (PAI) [4,5]. This imaging technique allows for the capture of vital information concerning blood vessels by employing a light source with specific wavelengths to determine the optical absorption properties of hemoglobin (Hb) [6,7]. Notably, the difference in the optical absorption properties of Hb is used to measure the oxygen saturation by

using light sources with wavelengths longer and shorter than the isosbestic point of oxy- and deoxyhemoglobin at 805 nm [8]. Currently, the majority of PA applications are related to morphological imaging, with the quantitative measurement of blood flow velocity yet to find widespread practical application. The twisting and turning of microvasculature within tumor blood vessels disrupt blood flow, hindering effective treatment. The quantitative measurement of blood flow velocity proves beneficial for identifying and assessing these disturbances in the blood flow [9].

Presently, the blood flow velocity is predominantly measured employing pulsed ultrasound Doppler velocimetry (UDV). UDV is widely used for medical diagnoses relatively deep inside the human body with its advantage of non-invasiveness without nuclear radiation [10]. Tang et al. conducted UDV-based imaging of blood velocity in the rodent brain with a time resolution of 100  $\mu$ s and a penetration depth exceeding 10 mm [11]. However, the spatial resolution of UDV is restricted by the low contrast due to small differences of acoustic impedance between biological tissues. On the other hand, in PA methods, a higher resolution is expected with a higher contrast due to the wavelength-dependent optical absorption of different biological tissues [12]. Fang et al. imitated UDV and developed PA Doppler velocimetry [13]. Another advantage of PA flow velocimetry is its signal enhancement capability with high repetition rate light sources. PA imaging has applied wavelength sensitivity to visualize lymphatic flow and oxygen saturation distributions [4], while signal enhancement was demonstrated by coding and decoding illuminations in PA measurements [14]. Notably, the PA method has the potential to determine the velocity of individual cells or particles using specific wavelengths. For instance, the ultrasound signals generated from red blood cells (RBCs) are not significantly affected by the refraction from the surrounding tissue. The PA method excels in measuring microvasculature velocity, which is challenging to measure accurately using conventional UDV due to low echogenicity [15]. Researchers have employed the PA Doppler effect to measure flow velocities using tracer particles [16,17].

In such PA velocimetry, the cross-correlation (CC) of pairs of PA signals has been proposed [18–21]. PA signal pairs generated from clusters of RBCs irradiated with pulsed lasers are measured at the ultrasound transducer (UST). The velocities of the clusters were measured by determining the time shift of the arrival signals with the peak of their CCs. One key advantage of the method is that, if the time delay between pulse irradiations is freely selected, it can measure a wide range of velocities compared to the Doppler method, which has limitations in the region of interest (ROI) and velocity range. Brunner and Beard [19] utilized a micro-scale absorber imprinted on an acetate sheet mounted on a rotating disk, and the rotational velocity was measured in a range of  $\pm 150$  to  $\pm 1500$  mm/s. Their results demonstrated the capability of measuring velocities up to 1400 mm/s with a resolution of  $\pm 8.0$  mm/s. The technique can be extended by considering the beam width of the UST and setting the time delay to 15 ms. However, the measurements were limited to the range of  $\pm 150$  to  $\pm 1500$  mm/s due to non-uniform motor speeds below 150 mm/s. While these measurements were conducted with multiple particles to mimic RBCs in blood, the performance of CC-based PA velocity measurements for a single object has not been adequately evaluated. Previous studies focusing on single particles or objects were conducted for verifying theoretical models [22]. The ability to measure the velocity of individual objects is essential for identifying single cells circulating at different velocities or cell aggregates, and to determine a cell's location in a vessel cross-section [23,24]. The flow velocity in the microvasculature was estimated to be  $< 50$  mm/s. Since the objective of the PA velocity measurement primarily targets lower speeds in the range of 10 mm/s, it is necessary to investigate the measurement performance for a single object at lower velocities such as in several  $\pm 10$  to  $\pm 100$  mm/s. Additionally the microvasculature exhibits a frequency component corresponding to the heartbeat. This implies that pulsation must be considered when measuring the flow velocity of the microvasculature [25].

In this study, we evaluated the performance and uncertainty associated with PA velocity measurements across a wide range of velocities, including both positive and negative directions. PA signals from micro-scale particles that are employed to simulate RBCs are weak and sensitive to background noise. Particularly in the case of particle clusters in fluid, the dispersion and diffusion of particle clusters, as well as their advection, contribute to the variation of the resulting PA signal pairs, which degrades the measurement performance. To evaluate the measurement performance of the advection due to the motion of the particle cluster, a high signal-to-noise ratio (SNR) and repeatability are required in the experiments. Our objective was to obtain PA signals that are not hidden by noise, which is crucial for the accurate assessment of PA velocity measurements. To achieve this, we employed a GC with a diameter of 2.0 mm as an object, given its efficient light energy absorption capabilities compared with that of RBCs, thereby generating PA signals with a high SNR with sufficient repeatability without the dispersion nor diffusion of particle clusters in fluid. Using a loudspeaker (LS) oscillation for generating repeatable sinusoidal linear motion, the movement of the object was facilitated in the range of  $-300$  to  $300$  mm/s. We evaluated the fundamental performance of the measurements and compared them with the reference velocities generated by the LS oscillation. The PA signals were generated from a GC by irradiating it with a pair of laser pulses with a time delay. The time shift between the signals was determined by employing CC in the time-domain, allowing for the calculation of velocity. The LS is capable of generating the velocities in a range of several 10 to 300 mm/s by adjusting the input voltage amplitude and frequency. In the experiment, a function generator was used to synchronize pulse repetition frequency (PRF) and LS oscillations. This synchronization enabled pulse irradiation at arbitrary positions in the LS oscillation by shifting their phases. Furthermore, the results of the measurement performance with a single object can be transferred to the experiment with multiple objects towards the PA flow velocimetry.

In the following sections, we outline the methodology, experimental apparatus and procedure, signal processing, results, and discussion. Section 2 describes the fundamental principles underlying the proposed method. Section 3 provides comprehensive details regarding the experimental apparatus utilized for velocity measurements employing the PA effect and a laser displacement sensor (LDS). Section 4 explains the experimental procedure and elucidates the signal processing method utilized for estimating the velocities. Section 5 discusses the experimentally determined velocities, resolution, and uncertainty of the velocities. Finally, Section 6 concludes the study, summarizing the findings and their implications.

## 2. Cross-Correlation Based Photoacoustic Velocity Measurement in Time-Domain

When a pair of pulsed lasers irradiates an object with a time delay  $t_p$ , a pair of PA signals is generated, denoted as  $p_1$  and  $p_2$ . In the scenario where the object remains stationary, only the original time delay  $t_p$  exists between the arrival time of the PA signal pair. Moreover, if no additional time shift  $t_s$  appears, the time delay  $\tau$  between the arrival time of the PA signal pair is expressed as  $\tau = t_p$ . However, if the object is in motion, as illustrated in Figure 1, a time shift  $t_s$  appears between the arrival time of the PA signal pair. The first PA signal  $p_1$  is generated by the first pulse irradiation. The second PA signal  $p_2$  arises from the object during motion after  $t_p$  seconds. Though  $p_1$  reaches UST promptly at time  $t = 0$  s,  $p_2$  arrives at the UST  $t_p \pm t_s$  seconds later due to the object's motion.

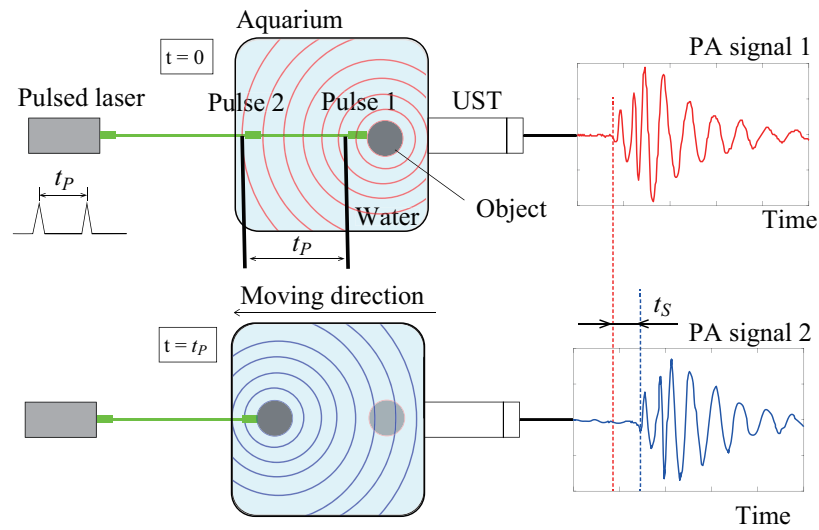


**Figure 1.** Principle of the velocity measurement using photoacoustic (PA) signals. PA signals are generated by irradiating an object with a pair of laser pulses separated by a pre-selected time delay  $t_p$ . When the time  $t = 0$  s, the first pulse generates PA signal 1. After  $t_p$  seconds, the second pulse irradiates the object, generating PA signal 2. During the  $t_p$  seconds, the object undergoes movements, causing a time-shift  $t_s$  in the arrival time of the PA signal pairs.

To determine the time shift  $t_s$  between a PA signal pair generated solely by an object’s movement, CC analysis was performed on the PA signal pairs  $p_1$  and  $p_2$ . CC analysis calculates the correlation between signals with a varying time delay and expresses it as a correlation coefficient. We assumed that the signals were correlated, and the correlation coefficient demonstrates the highest correlation at a certain time delay. The time shift  $t_s$  can be ascertained by identifying the peak correlation coefficient. This time shift represents the time difference between the arrival of the extracted PA signals at the UST. Utilizing this information, the propagation distance  $d$  of the PA wave is subsequently calculated as

$$d = t_s c. \tag{1}$$

where  $c$  represents the speed of sound in the medium. When considering the angle between the UST and the object as  $\theta$ , the propagation distance of the PA waves to the receiver is expressed as  $d = l \cos \theta$ , where  $l$  corresponds to the actual distance the object has moved. By dividing the displacement  $d$  by the time shift  $t_s$ , the velocity  $v$  of the object is computed as follows:

$$v = \frac{l}{t_p} = \frac{d}{t_p \cos \theta} = \frac{t_s c}{t_p \cos \theta}. \tag{2}$$

This is analogous to the classical equation of the Doppler frequency derived for a moving object, with the key distinction being that the velocity is now proportional to the time shift rather than the frequency shift [19,21]. The proposed method enables the estimation of both the object’s moving velocity and direction of movement using the time shift  $t_s$  obtained from the CC analysis of the PA signal pair. A CC function was employed to determine the time shift  $t_s$  between the two PA signals,  $p_1$  and  $p_2$ . By taking the complex conjugate of  $p_1$  as  $p_1^*$ , the continuous function for CC is defined as follows:

$$(p_1 \star p_2)(t) = \int_{-\infty}^{\infty} p_1^*(\tau) p_2(t - \tau) d\tau. \tag{3}$$

For discrete signals  $p_{kn}$ , where  $k = 1, 2$ , and the number of samples is  $n = 0, \dots, N - 1$  with  $N$  the total number of samples and a time separation of  $\Delta t$ , the relationship between the continuous signal  $p_k(t)$  and the discrete signals  $p_{kn}$  is defined as  $p_{kn} \equiv p_k(t)|_{t=n\Delta t}$ . The

CC results can be interpreted as the deterministic correlation between two deterministic signals. Then, for these discrete samples of length  $N$ , the CC function is defined as follows:

$$\hat{R}_{p_1 p_2}(m) = \begin{cases} \sum_{n=0}^{N-m-1} p_{1(n+m)} p_{2n}^* & (\text{for } m \geq 0), \\ \hat{R}_{p_2 p_1}^*(-m) & (\text{for } m < 0) \end{cases} \quad (4)$$

The output vector is denoted as  $c(m) = \hat{R}_{p_1 p_2}(m - N), m = 1, \dots, 2N - 1$ . The parameter  $m$  signifies the lag of the index between  $p_{1(n+m)}$  and  $p_{2n}$ , and is expressed as the number of samples, with the output vector  $c(m)$  being an output vector of the CC at lag  $m$ .

### 3. Experimental Apparatus

#### 3.1. PA Measurement

Figure 2 presents the setup used for PA measurements. A pair of independently controlled Q-switched neodymium-doped yttrium aluminum garnet (Nd:YAG) lasers emitting at 532 nm (Rayture Systems Co. Ltd., Tokyo, Japan, GAIA Dual) was employed to generate laser pulses. The time delay between the first and second pulses was pre-selected using a delay generator (Quantum Composers Inc., Bozeman, MT, USA, 9618+). The typical pulse energy was 9.0 mJ, and the pulse duration was 10 ns (full-width at half-maximum). The timings of the laser irradiation  $t_1, t_2$  were detected by a photodetector (PD) (Thorlabs Inc., Newton, NJ, USA, DET10A2) capable of detecting wavelengths ranging from 200 to 1100 nm. These data from the PD facilitated the calculations of the actual time delay  $t_p$  between the first and second pulses. A pair of laser pulses was aligned colinearly in the same region and adjusted to the same height as of an UST (Olympus Medical Inc. (now Evident Corporation), Tokyo, Japan V311-SU). The PRF was controlled using a two-channel function generator (RIGOL Technologies Inc., Suzhou, China, DG1022Z). The phase difference  $\varphi$  between the pulse and LS signals was also adjusted with the generator, enabling the irradiation of laser pulses at arbitrary timing with a sinusoidal period. The generated PA waves were detected by the UST with a center frequency of 10 MHz. The UST was connected to an oscilloscope via an amplifier (FEMTO Messtechnik GmbH, Berlin, Germany, HVA-10M-60-B). The detection angle  $\theta$  of the UST was adjusted to acquire the maximum amplitude of the PA signal. The acquisition of the PA signals was triggered at the first pulse irradiation based on the PD.

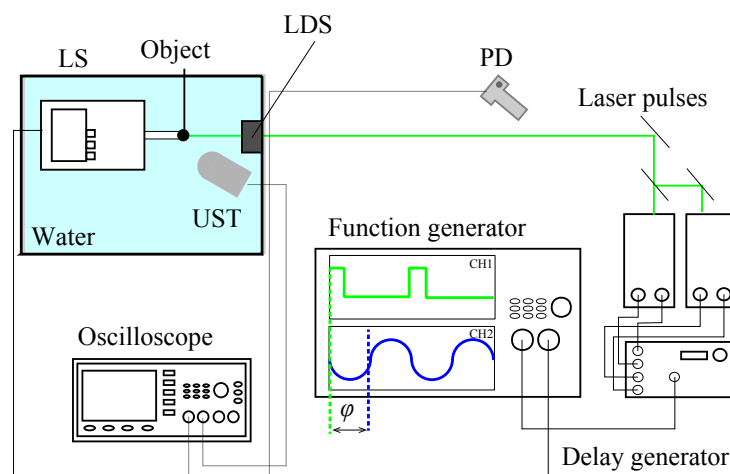


**Figure 2.** Experimental setup of the PA velocity measurement (PD: photo detector, PRF: pulse repetition frequency, LS: loudspeaker, UST: ultrasound transducer). A pair of pulsed lasers was irradiated an object immersed in the water. The object, a GC, was affixed to the LS membrane via an arm. The pre-selected time delay was controlled by the delay generator. The irradiation timings were detected by the PD. The PRF and LS oscillation were regulated via the function generator. The generated PA signals were measured employing the oscilloscope through the UST.



### 3.2. Loudspeaker System

Figure 3 depicts the experimental apparatus designed to generate object velocities. A GC with a diameter of 2.0 mm, containing carbon particles functioning as absorbers, served as the object. Positioned at the end of an arm attached to the LS membrane, the object was immersed in water, and oriented perpendicular to the free surface of the aquarium. We adjusted the amplitude  $A$ , frequency  $f$ , and phase difference  $\varphi$  of the input sinusoidal signal to drive the LS using a function generator. The signal to the LS was expressed as  $x = A \sin(2\pi f + \varphi)$ . The velocity of the object was directly proportional to the oscillation amplitude  $A$  and frequency  $f$ . The LS generated collinear motions along the optical axis of the pulsed lasers and the LDS, ensuring precise alignment between the motions and the optical axis.

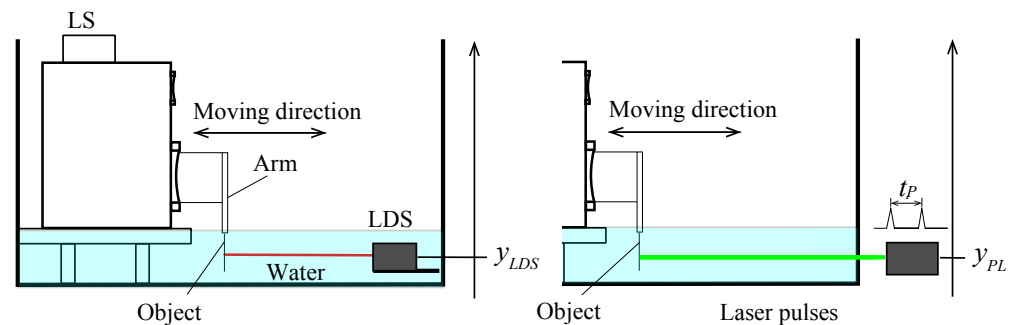


**Figure 3.** Experimental setup for LDS measurement. The object was set to a cantilevered arm, and the LDS was carefully submerged in water aligned to the optical axis of the pulsed lasers. The sinusoidal linear motion of the object was operated by the LS. The object displacement was measured using the LDS aligned collinear to the irradiation axis of the laser pulses.

We used an LDS (Optex FA Co. Ltd., Kyoto, Japan, CD22-15VM12) to measure the object displacement collinearly to the irradiation axis of the laser pulses, as shown in Figure 3. The repeatability of the LDS was specified as 1.0  $\mu\text{m}$ . The timing of the data acquisition was triggered by the first pulse irradiation, enabling synchronization with the PA measurements. The displacement obtained from the LDS was acquired directly using the oscilloscope. Subsequently, the acquired data were processed on a personal computer (PC) to convert them into object velocity. The velocity acquired from the LDS served as a reference for the PA velocity measurement, enabling the comparison and evaluation of the uncertainty of the PA velocity measurements.

## 4. Experimental Methods

### 4.1. PA Signal Analysis

To acquire a pair of PA signals, the object was irradiated using pulsed lasers with a time delay of  $t_p = 1.0$  ms. The PRF and oscillation of the LS were regulated at a frequency of 5 Hz. To acquire the velocities within one oscillation period, the phase difference  $\varphi$  between the pulse and LS signal was adjusted in the range of  $0^\circ$  to  $360^\circ$ .

Figure 4a presents a typical pair of the PA signals and the corresponding PD data. The first pulse of irradiation generated the first PA signal. As the object moves during the time delay  $t_p$ , the second pulse irradiation generated a second PA signal. The timing of each pulse irradiation denoted as  $t_1$  and  $t_2$  was determined by applying a central-difference scheme to the PD signal recorded at the measurement. The maximum value acquired from the central-difference result was considered as the timings  $t_1$  and  $t_2$ , as shown in Figure 4b. Subsequently, a pair of PA signals  $p_1$  and  $p_2$  were extracted based on these timings, as depicted in Figure 4c. The time difference between  $t_1$  and  $t_2$  was calculated as  $t_p = t_2 - t_1$  for each measurement. CC analysis was then applied to the extracted pair of PA signals  $p_1$  and  $p_2$ . Figure 4d illustrates CC analysis results, where the peak of the correlation coefficient represented the horizontal position with the highest correlation between PA

signal pairs. The time shift  $t_s$  between the PA signal pair arriving at the UST was calculated based on the correlation peak.

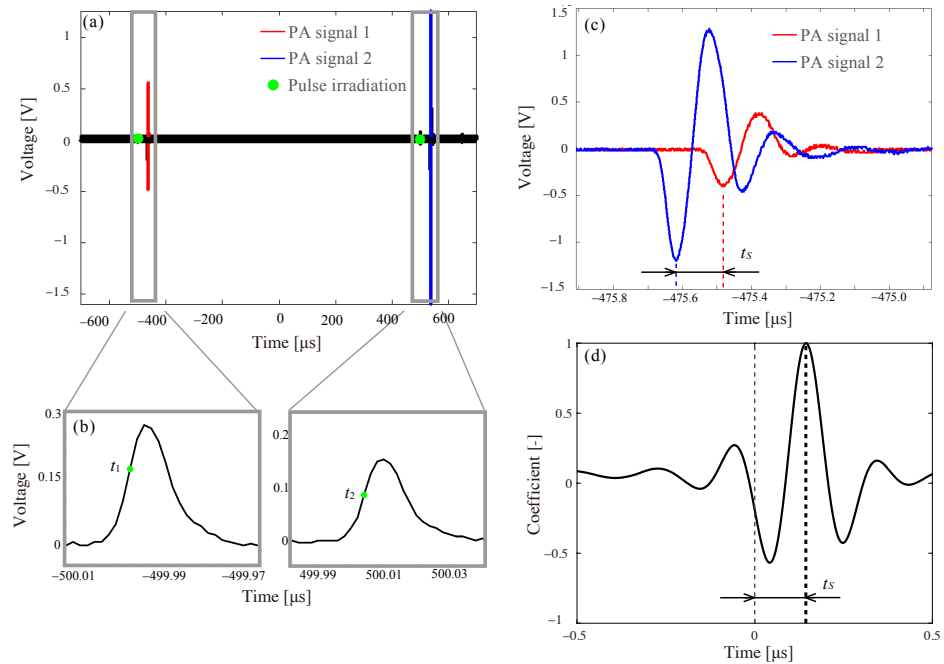


**Figure 4.** Typical PA and PD signals in time domain. (a) PA and PD signals with a time delay  $t_p$ . The red signal represents an extracted PA signal 1 from the first pulse irradiation, while the blue one illustrates an extracted PA signal 2 generated from the second pulse irradiation. (b) The pulse irradiation timings  $t_1, t_2$  detected by the central-difference of the PD signals. (c) Comparison of the extracted PA signals. The extraction timings were the irradiation timings  $t_1, t_2$ . The time shift  $t_s$  was calculated based on the CC of the extracted signals. (d) CC results of the extracted signals with the peak position defined as time shift  $t_s$ .

First, calibration experiments were conducted under stationary conditions of the object. This was performed to investigate the limiting measurement uncertainty of the system. Then, we performed a series of PA velocity measurements of an object in sinusoidal linear motion. The phase difference of the PA measurement was adjusted every  $5^\circ$  to cover the whole range from  $\varphi = 0^\circ$  to  $360^\circ$ . In both experiments, the pre-selected time delay between pulse irradiations  $t_p$  was set to  $t_p = 1.0$  ms.

#### 4.2. Displacement Analysis

The acquired displacement  $A$  was converted to a velocity as a reference for the PA measurement. In the ideal case where the LS output follows an analytical form, it is possible to estimate the velocity  $v_{ideal}$  as follows:

$$v_{ideal} = 2\pi f A \cos(2\pi f t + \varphi). \tag{5}$$

However, the behavior of the LS oscillation changed owing to the influence of the arm, which is particularly notably in the behavior changes at the folding back of the oscillation. Consequently, the acquired output signal differs from the input signal. To overcome this, we employed a central-difference scheme [26] to calculate the velocity from the positional information. In the discrete form, the velocity  $v_{LDS}(i\Delta t)$  at an index  $i (= 1, 2, \dots, N)$  was obtained as

$$v_{LDS}(i\Delta t) = \frac{LDS\{(i+1)\Delta t\} - LDS\{(i-1)\Delta t\}}{2\Delta t}, \tag{6}$$

with  $\Delta t$  being the time increment and  $N$  being the total number of the samples. At the first  $i = 1$  and last points  $i = N$ , we applied the forward and backward difference scheme, respectively.

The velocities were obtained from the displacement data acquired with the LDS at different sample frequencies. The trigger for signal acquisition was set to the first pulse of irradiation. From this trigger point, velocities  $v_{LDS}$  were computed for half or one oscillation. The measurements were conducted five times under identical experimental conditions to ensure accuracy and consistency.

## 5. Results and Discussions

### 5.1. Calibration Experiment

In the calibration experiment, the detected pulse irradiation timings were  $t_1 = 0$  ms and  $t_2 = 1.0$  ms. The calculated time delay  $t_p$  based on the pulse irradiation timings was determined to be  $t_p = t_2 - t_1 = 1.0$  ms. The PA signals were extracted based on the pulse irradiation timings  $t_1$  and  $t_2$ , and CC analysis was applied to the extracted signals. The peak of the CC coefficient was determined at a time shift  $t_s = -0.0040$   $\mu$ s. The relevant parameters employed in the calculations were  $\theta = 30^\circ$  and  $c = 1.5 \times 10^6$  mm/s at 22 °C. Based on Equation (2), the velocity of the stationary object was evaluated as

$$v_0 = \frac{t_s c}{t_p \cos \theta} = \frac{1.50 \times (-0.0040)}{1.0 \times 10^{-3} \times \cos 30^\circ} = -6.9 \text{ mm/s.} \quad (7)$$

The ensemble average of 10 samples measured for the stationary case yielded an average velocity of  $v_{\text{avg}} = -3.4$  mm/s. The standard deviation (SD) of the PA velocity measurements was calculated as  $\sigma_{v_0} = 5.0$  mm/s. The velocity resolution was limited by the sample rate of the digitizer of the measurement instrument, i.e., the oscilloscope. Under the experimental conditions, the minimum measurable velocity  $v_{\text{lim}}$  was calculated as  $v_{\text{lim}} = \pm 3.4$  mm/s by substituting the sampling interval of the measurement instrument  $t_s = 0.002$   $\mu$ s into Equation (2). Theoretically,  $v_{\text{avg}}$  is 0 mm/s in the stationary case. However, in the experiment, the velocity measured for a stationary object ( $v_{\text{avg}} = -3.4$  mm/s), was within the minimum measurable velocity ( $v_{\text{lim}} = \pm 3.4$  mm/s), indicating the reasonableness of the PA velocity measurement.

### 5.2. PA Velocity Measurement

In the PA velocity measurement, the detected time delay  $t_p$  was obtained as  $t_p = t_2 - t_1 = 1.0$  ms using the PD. The peak of the CC coefficient acquired was determined at a time shift of  $t_s = 0.14$   $\mu$ s. Using Equation (2), the velocity of the object oscillated by the LS was calculated as

$$v = \frac{t_s c}{t_p \cos \theta} = \frac{1.5 \times 0.14}{1.0 \times 10^{-3} \times \cos 30^\circ} = 241 \text{ mm/s.} \quad (8)$$

Figure 5 illustrates the results of the velocities obtained from the PA measurements ranging from  $-300$  to  $300$  mm/s. The black dots represent velocities measured at  $5^\circ$  intervals in the phase difference  $\varphi$ . The green line indicates the moving average of the PA measurements. The maximum velocity  $v = 316$  mm/s was recorded at  $\varphi = 10^\circ$ , corresponding to a time of 5.6 ms. The negative maximum velocity  $v = -292$  mm/s was obtained at  $\varphi = 190^\circ$ , which corresponds to a time of 0.11 s.

The object oscillates sinusoidally at 5 Hz and completes one period every 0.20 s. The input sinusoidal signal undergoes a phase reversal every  $180^\circ$ , which corresponds to a time of 0.10 s. The time difference between the two maximum velocities was 0.10 s, which is equivalent to half of a sinusoidal oscillation period. There is folding back of the LS oscillation at 0.055 s, resulting in significant velocity changes due to arm bending. The results indicate that the phase-resolved object motion is captured in the range of  $-300$  to  $300$  mm/s at a frequency of 5 Hz.



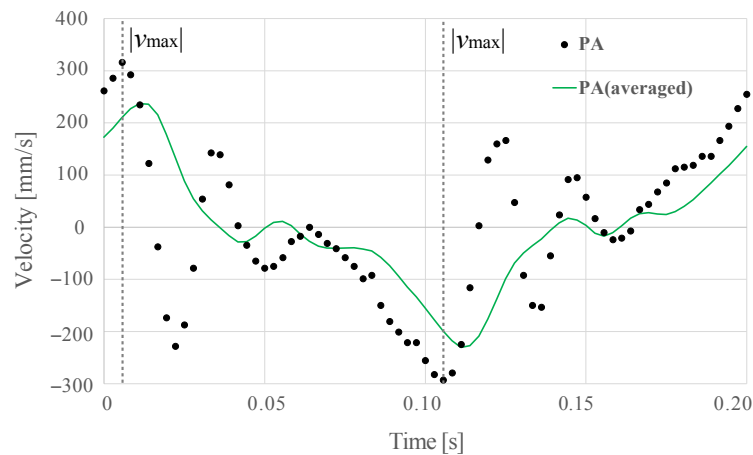


**Figure 5.** Result of PA velocity measurement with 5° interval. The object underwent sinusoidal oscillation at 5 Hz, completing one period every 0.20 s. The black dots represent the velocities obtained from the PA velocity measurement, while the green line illustrates the averaged velocities of PA measurement. The positive maximum velocity  $v_{\max} = 316$  mm/s was recorded at 5.6 ms, while the negative maximum velocity  $v_{\max} = -292$  mm/s was obtained at 0.11 s.

### 5.3. LDS Velocity Measurement

Figure 6 displays the results of the acquired displacement and reference velocity. The measurements were conducted five times under the same conditions, and the reference velocity was taken as the average of the measurements. Notably, the shape of the displacement does not exhibit ideal sinusoidal linear motion due to the inherent characteristics of the LS. When an amplified signal was directed to the LS, the displacement of the voice-coil inside the LS increased and became nonlinear. This nonlinearity led to distortions in the displacement, as evident in Figure 6. Furthermore, distortions in the displacement were caused by arm bending. When the arm was cantilevered, the oscillation exhibited a folding back point near the maximum displacement. At the maximum displacement  $A = 3.4$  mm, the velocity of the object appeared to be  $-1.2$  mm/s, as depicted in Figure 6.

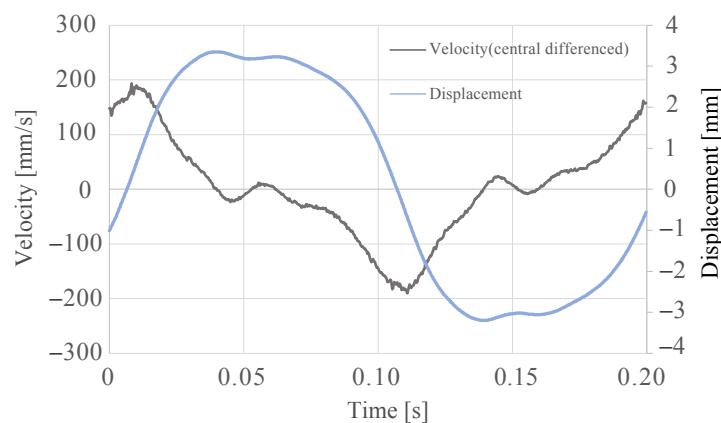


**Figure 6.** Result of LDS measurement. The blue line indicates the displacement of the object, while the gray line depicts the velocities calculated using a central-difference scheme of the displacement data. The positive maximum velocity reached  $v = 194$  mm/s at 8.3 ms, and the negative maximum velocity was  $v = -191$  mm/s at 0.11 s.

The velocities were calculated as a second-order central-difference of the displacement data obtained by the LDS. The maximum reference velocity  $v = 194$  mm/s was determined at a time of 8.3 ms, which was considered as reference position of the LS. The negative maximum reference velocity  $v = -191$  mm/s was acquired at a time of 0.11 s. The maximum reference velocity was estimated as being 39% lower than that acquired from the PA result.

As discussed in the next section, this deviation is due to the averaging included in the LDS. The SD of velocity measurements ranged from 0.32 to 7.8 mm/s. A relatively large SD was obtained at around 200 mm/s.

#### 5.4. Comparison of the Results

Figure 7 compares the results obtained from the LDS and PA measurements. Each measurement was conducted five times under the same conditions, and the average velocity and SD were calculated. Notably, the velocity measured by the LDS was moving-averaged in advance within the instrument, necessitating the PA result to be moving-averaged. The green line PA(averaged) showcases the moving average velocities from the PA measurement, with the results indicating consistent velocity variations even during the folding back of the oscillation at 0.055 s. The acquired movements were consistent for both measurements.

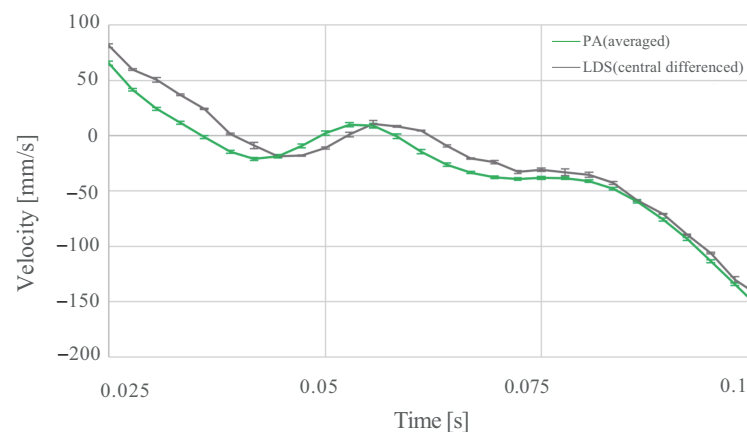


**Figure 7.** Comparative analysis of the measurement results based on the PA and the LDS. The gray line indicates the velocity measured by the LDS, while the green line represents the averaged velocities derived from the PA result. Notably, the LS oscillation exhibited a folding back at 0.055 s in all measurements. The PA measurement uncertainties ranged from 0.86 to 2.1 mm/s. The maximum deviation between the LDS and PA was 26 mm/s at 0.031 s.

The maximum deviation between the LDS and PA was 26 mm/s at 0.031 s, primarily attributed to the temporal resolution of the respective measurements. The resolution of the LDS varied from 0.50 to 4.0 ms, while that of the PA was 2.8 ms. The resolution of the PA depends on the phase difference  $\varphi$  between LS and pulse signal and could potentially be improved up to 0.56 ms. By aligning the temporal resolution of both measurements, the deviation should be further reduced. The statistical uncertainties of the PA velocity measurement were calculated as 0.86 to 2.1 mm/s in the measurements. The average velocity  $v = -155$  mm/s was calculated at 0.10 s, the absolute uncertainty at 0.86 mm/s and the relative uncertainty at 0.56%. At an average velocity  $v = 9.0$  mm/s at 0.055 s, the absolute uncertainty was 2.1 mm/s and the relative uncertainty was 24%. The large relative uncertainty at low velocities was attributed to the minimum measurable velocity determined by the sample rate of the digitizer of the measurement instrument. This limitation could be overcome by interpolating the CC coefficient for peak determination [27].

Figure 8 showcases the comparison of the results acquired from the LDS and PA measurements in the range of  $-50$  to  $50$  mm/s. The PA data were an ensemble average of five measurements. Comparing only the PA data with Figure 5, the velocity distribution in Figure 8 is similar to a cosine waveform. This is consistent with the fact that, theoretically, the output signal of the input sine signal is a cosine waveform. In addition, the positive maximum velocities were obtained around 0 and 0.20 s, and the negative maximum velocity was obtained around 0.10 s, which is consistent with the theoretical cosine waveform. We applied a time average to the PA results for comparing them with the LDS results internally averaged in the instrument. Figure 8 shows the comparison of the results with the moving average. While the LDS results were the average of every 64 samples with the sampling

frequency at 0.5 ms, the PA results were averaged over 12 neighbor points, which were measured at the time resolution of 2.72 ms. As a result, PA (averaged) data are observed to be shifted 33 ms to the right side from the original PA data. This result indicates that the PA (averaged) data of velocity distribution with the SD are generally consistent with the LDS data. Relatively large deviation observed around the maximum velocities is expected due to the underestimation occurring with the application of the central-difference scheme to the LDS data. Moreover, the consistency of the results was experimentally confirmed in velocity measurements with two additional cases described in Appendix A. The two cases include the object with a GC with a smaller diameter of 0.5 mm and with multiple cylinders with smaller diameters of 0.5 mm. These results indicate that the PA velocity measurement was able to monitor the movement of the object faithfully. The PA (averaged) data were consistent with the LDS data, indicating that the PA measurements without moving average were able to measure local movements that were not resolved in the LDS measurements.

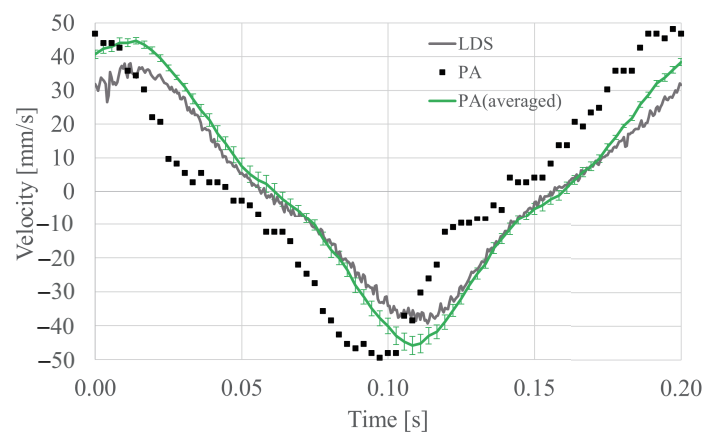


**Figure 8.** Comparison of velocities measured using the PA and LDS in the range of 0 to 100 mm/s. The input signal to the LS was a sinusoidal waveform, with the resulting displacement measured with the LS being a cosine waveform. The PA data showcase the maximum velocities at the theoretical phases. The folding back of the LS oscillation occurs at 0.05 and 0.15 s, where velocities approach 0 mm/s. The LDS data were internally averaged before the output. The PA data were moving averaged over 12 neighbor points to match the temporal resolution of the LDS data. As a result, the PA (averaged) data shifted 0.033 s to the right.

## 6. Conclusions

We investigated the performance of the PA velocity measurement of an object in one-dimensional motions. The PA signals were generated by irradiating the pulsed lasers with a pre-selected time delay. The object velocity was measured by calculating the time shift between the PA signal pairs using CC in the time domain. For the calibration experiment, the average velocity of the stationary object was calculated as  $v_{\text{avg}} = -3.4$  mm/s, which was consistent with the minimum measurable velocity  $v_{\text{lim}} = \pm 3.4$  mm/s of the measurement system. To evaluate the dynamic performance, we employed the linear sinusoidal motion of a single GC attached to an LS membrane. The periodic linear motions resulted in reproducible linear velocities with a range of  $-300$  to  $300$  mm/s. Motion was independently monitored by the LDS, which provided the reference velocity of the moving object. The PA measurement results provided the phase-resolved velocities of the object monitored by the LDS measurement. The results suggested that the measurement uncertainties were consistent with the values in the stationary case and remained almost constant over the investigated velocity range. Furthermore, the PA measurements revealed the local fine velocities of the object which were not resolved by the LDS measurements. A comparison of the LDS and PA results revealed deviations in the shape of the output waveform from the input signals. The nonlinearity in the LS output and distortions caused by arm bending contributed to these deviations. Despite these deviations, the PA results faithfully captured velocity variations in the range of  $-200$  to  $100$  mm/s, even during the folding back of the LS oscillation. The fold-

ing back was acquired at 0.055 s and the maximum deviation between the LDS and PA was 26 mm/s at 0.031 s. This deviation was attributed to the temporal resolution determined by the sampling rate at the measurement. The deviation could be reduced by increasing the temporal resolution and/or applying interpolation to the correlation coefficients in the determination of the peak location. The uncertainty of the PA velocity measurements ranged from 0.86 to 2.1 mm/s for the maximum and minimum velocities, respectively. Furthermore, the PA measurements revealed the local fine velocities of the object, which were not resolved by the reference velocities of the LDS measurements. The capability of the PA velocity measurement is expected to be advantageous in blood velocimetry measurements with dynamic variations in both magnitude and direction. This offers the prospect of mapping in a multi-dimensional region, although the present study is limited to a single object in a one-dimensional case. Further investigation is necessary to ensure the feasibility of the clustered RBCs at a micrometer scale in the microvascular environment.

**Author Contributions:** Conceptualization, K.F. and K.S.; Methodology, K.F. and K.S.; Validation, K.F.; Investigation, K.F.; Writing—original draft, K.F.; Writing—review & editing, K.S.; Supervision, K.S.; Funding acquisition, K.S. All authors have read and agreed to the published version of the manuscript.

**Funding:** This research received no external funding.

**Institutional Review Board Statement:** Not applicable.

**Informed Consent Statement:** Not applicable.

**Data Availability Statement:** The data presented in this study are available on request from the corresponding author. The data are not publicly available due to privacy.

**Conflicts of Interest:** The authors declare no conflict of interest.

## Appendix A. Examinations of Smaller-Sized Cylinders and Multiple Cylinders

### Appendix A.1. Experiment Configuration

In the main text, we investigated the measurement performance with only a single cylinder with a specific diameter. In this appendix, we investigate the consistency of the results of PA velocity measurement with respect to the light-absorbing cylinder. The measurements were performed in two cases, one with a smaller cylinder and another with multiple cylinders. In the first case, we employed a single GC with a diameter of 0.5 mm, which was smaller than the one employed in the main text. In the second case, an object consisting of three GCs with a diameter of 0.5 mm aligned laterally with center-to-center distances 0.6 mm each other. Figure A1 illustrates the experimental configurations. The conditions and procedures were identical to the one performed for the single GC with a diameter of 2.0 mm in the main text. In each experiment, measurements were repeated five times and the ensemble averages were analyzed. Figure A2 compares the results with a single GC at a diameter of 2.0 mm (black) and at a diameter of 0.5 mm (blue), and with the three GCs at a diameter of 0.5 mm (orange).

### Appendix A.2. Effect of the Object Size

The effect of the object size is considered by examining the results of a single GC with the two different diameters plotted in Figure A2. While the plots in black dots indicate the result of 2.0 mm, the blue dots shows that of 0.5 mm. Comparing these, the result at 0.5 mm exhibits systematic deviation in the positive velocity direction, meaning that a higher velocity is obtained with the smaller diameter than with the larger one. This was attributed to the systematic deviation of the detection angle  $\theta$ , which had a larger contribution for the smaller diameter case. In the positive direction, when the object moves close to the UST, a consistently faster velocity is obtained. On the other hand, in the negative direction, when the object moves away from the UST, a consistently slower velocity is obtained. The

sensitivity of the detection angle increases for the smaller diameter. Nevertheless, the result of the smaller diameter at 0.5 mm exhibits the same tendency as the larger one at 2.0 mm.

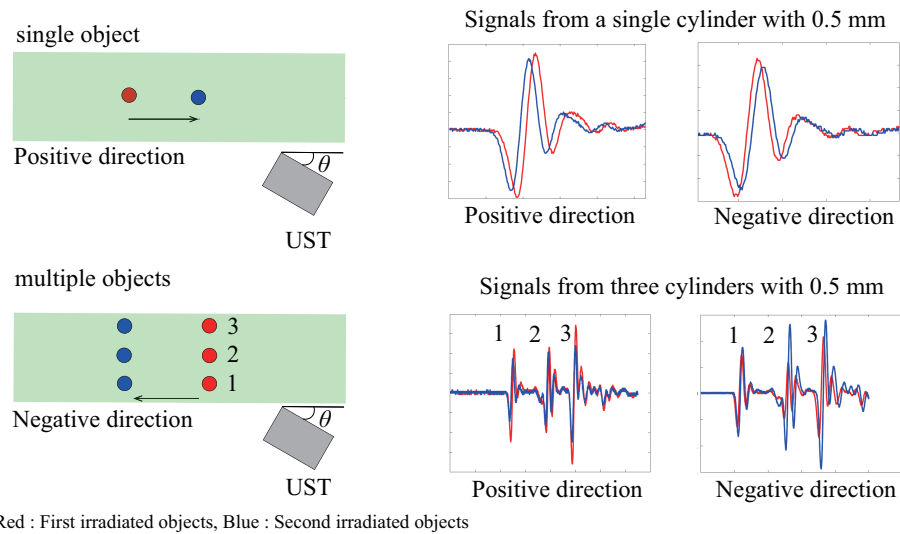


**Figure A1.** Experimental setup for the comparative measurement. PA velocity measurements were conducted with two cases of the light absorbing objects with a single GC at a diameter of 0.5 mm and with three GCs at a diameter of 0.5 mm aligned laterally. In the positive direction of the movement toward the UST, the second PA signal (blue) arrived at the UST earlier than the first one (red).

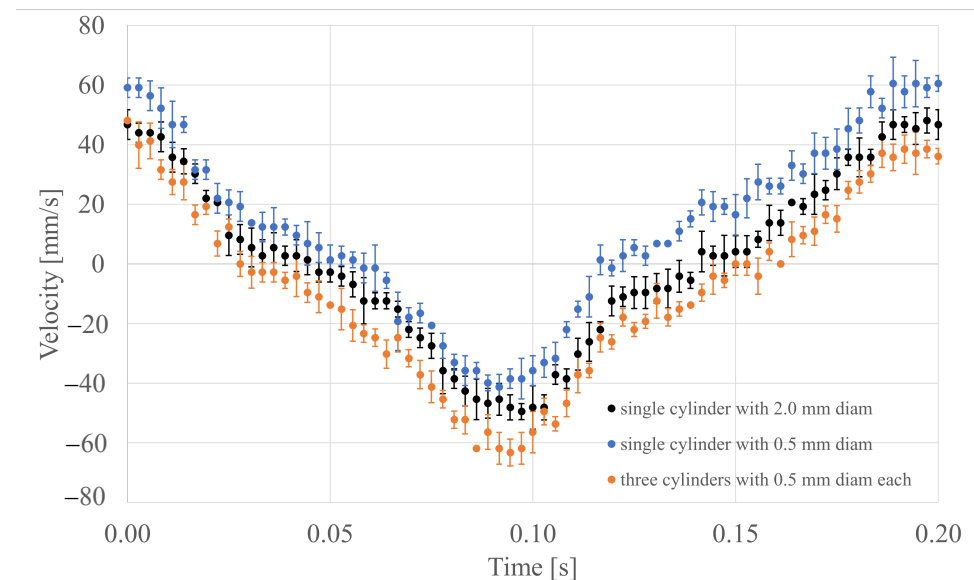


**Figure A2.** Result of PA velocity measurement with 5° interval. The object was oscillated sinusoidally at 5 Hz, completing one period every 0.20 s. The blue dots show the velocities of a GC with a diameter of 0.5 mm; the black dots show the 2.0 mm cylinder. Additionally, the orange dots show the velocity results of three cylinders with a diameter of 0.5 mm. These results are the ensemble average of five measurements. The SDs are shown as error bars.

*Appendix A.3. Effect of a Single Cylinder or Multiple Cylinders*

The effect of the single or multiple cylinders is considered by examining the results of the single GC and multiple GCs plotted in Figure A2. While the plots with black and blue dots indicate the results of a GC with a diameter at 2.0 mm or 0.5 mm, the plot with orange dots indicates the results of the three GCs. Comparing these, the result of the three cylinders exhibits systematic deviation in the negative velocity direction, meaning that a smaller velocity is obtained than in the single cylinder case. This is explained with the

difference in the position at which PA signals are generated in each of them, as shown in Figure A1. The PA signal 1 (marked in the bottom right) generated by cylinder 1 is the closest to the UST, while the PA signal 3 generated by cylinder 3 is the farthest from the UST. In the case of the positive direction, a smaller velocity was consistently estimated compared to those of the single cylinder cases. In the case of cylinder 1 in the positive direction, the time shift between the two PA signals (red and blue) was relatively large, indicating that cylinder 1 moved closer to the UST at a relatively fast velocity (about 60 mm/s). In contrast, focusing on PA signal 3, the time shift between the two PA signals was smaller than that of the PA signal 1; cylinder 3 moved closer to the UST (about 40 mm/s). This is attributed to the fact that cylinder 1 was located closer to the UST, while cylinder 3 was far from the UST in comparison. The result is shifted in the positive direction when the cylinders are close to the UST. Accordingly, when the cylinders are far from the UST, as with cylinder 3, the result is shifted in the negative direction. In the present configuration, the PA signal from cylinder 3 is largest and the result of CC is biased towards cylinder 3. Consequently, the result of the three cylinders is biased to cylinder 3. From these results, the effect of the angle was found to be crucial for the measurement. When the size of the object is downsized or the number of objects is increased, the angle of the UST and the distance to the object need to be adjusted carefully. When the probe and objects are set far from each other, the effect of the angle change during movement is estimated to be small, but the signal intensity is reduced, resulting in a deterioration of the SNR. Consequently, it is necessary to extract only the signal of interest with relatively high intensity by minimizing the irradiation spot or by using a focused UST probe.

## References

1. Wang, L.H.V.; Wu, H. *Biomedical Optics: Principles and Imaging*; Wiley: Hoboken, NJ, USA, 2007. [[CrossRef](#)]
2. Wang, L.; Zhang, C.; Wang, L.H.V. Grueneisen relaxation photoacoustic microscopy. *Phys. Rev. Lett.* **2014**, *113*, 1–12. [[CrossRef](#)] [[PubMed](#)]
3. Manohar, S.; Razansky, D. Photoacoustics: A historical review. *Adv. Opt. Photonics* **2016**, *8*, 586–617. [[CrossRef](#)]
4. Nagae, K.; Asao, Y.; Sudo, Y.; Murayama, N.; Tanaka, Y.; Ohira, K.; Ishida, Y.; Otsuka, A.; Matsumoto, Y.; Saito, S.; et al. Real-time 3D photoacoustic visualization system with a wide field of view for imaging human limbs. *F1000Research* **2019**, *7*, 1813. [[CrossRef](#)] [[PubMed](#)]
5. Matsumoto, Y.; Asao, Y.; Yoshikawa, A.; Sekiguchi, H.; Takada, M.; Furu, M.; Saito, S.; Kataoka, M.; Abe, H.; Yagi, T.; Togashi, K.; Toi, M. Label-free photoacoustic imaging of human palmar vessels: A structural morphological analysis. *Sci. Rep.* **2018**, *8*, 786. [[CrossRef](#)]
6. Jansen, K.; Wu, M.; van der Steen, F.W.A.; van Soest, G. Lipid detection in atherosclerotic human coronaries by spectroscopic intravascular photoacoustic imaging. *Opt. Express* **2013**, *21*, 21472–21484. [[CrossRef](#)] [[PubMed](#)]
7. Liu, C.; Wang, L. Functional photoacoustic microscopy of hemodynamics: A review. *Biomed. Eng. Lett.* **2022**, *12*, 97–124. [[CrossRef](#)] [[PubMed](#)]
8. Esenaliev, R.O.; Larina, I.V.; Larin, K.V.; Deyo, D.J.; Motamedi, M.; Prough, D.S. Optoacoustic technique for noninvasive monitoring of blood oxygenation: A feasibility study. *Appl. Opt.* **2002**, *41*, 4722–4731. [[CrossRef](#)] [[PubMed](#)]
9. Brunker, J.; Beard, P. Velocity measurements in whole blood using acoustic resolution photoacoustic Doppler. *Biomed. Opt. Express* **2016**, *7*, 2789–2806. [[CrossRef](#)]
10. Hein, A.I.; O'Brien, D.W. Current time-domain methods for assessing tissue motion by analysis from reflected ultrasound echoes—A Review. *IEEE Trans. Ultrason. Ferroelectr. Freq. Control* **1993**, *40*, 84–102. [[CrossRef](#)]
11. Tang, J.B.; Postnov, D.D.; Kilic, K.; Erdener, S.E.; Lee, B.; Giblin, J.T.; Szabo, T.L.; Boas, D.A. Functional Ultrasound Speckle Decorrelation-Based Velocimetry of the Brain. *Adv. Sci.* **2020**, *7*, 2001044. [[CrossRef](#)]
12. Xu, M.H.; Wang, L.H.V. Photoacoustic imaging in biomedicine. *Rev. Sci. Instrum.* **2006**, *77*, 041101. [[CrossRef](#)]
13. Fang, H.; Maslov, K.; Wang, L.H.V. Photoacoustic Doppler effect from flowing small light-absorbing particles. *Phys. Rev. Lett.* **2007**, *99*, 184501. [[CrossRef](#)] [[PubMed](#)]
14. Zhang H.K.; Kondo, K.; Yamakawa, M.; Shiina, T. Coded excitation using periodic and unipolar M-sequences for photoacoustic imaging and flow measurement. *Opt. Express* **2016**, *24*, 17–29. [[CrossRef](#)] [[PubMed](#)]
15. Zangabad, P.R.; Iskander-Rizk, S.; van der Meulen, P.; Meijlink, B.; Kooiman, K.; Wang, T.; van der Steen, F.W.A.; van Soest, G. Photoacoustic flow velocity imaging based on complex field decorrelation. *Photoacoustics* **2021**, *22*, 100256. [[CrossRef](#)] [[PubMed](#)]
16. Sheinfeld, A.; Gilead, S.; Eyal, A. Simultaneous spatial and spectral mapping of flow using photoacoustic Doppler measurement. *J. Biomed. Opt.* **2010**, *15*, 066010. [[CrossRef](#)] [[PubMed](#)]
17. Zhang, R.; Yao, J.; Maslov, I.K. Structured-illumination photoacoustic Doppler flowmetry of axial flow in homogeneous scattering media. *Appl. Phys. Lett.* **2013**, *103*, 094101. [[CrossRef](#)] [[PubMed](#)]



18. Liang, J.; Zhou, Y.; Maslov, I.K.; Wang, L.H.V. Cross-correlation-based transverse flow measurements using optical resolution photoacoustic microscopy with a digital micromirror device, resolution and scalability. *J. Biomed. Opt.* **2013**, *18*, 1780–1791. [[CrossRef](#)] [[PubMed](#)]
19. Brunker, J.; Beard, P. Pulsed photoacoustic Doppler flowmetry using time-domain cross-correlation: Accuracy, resolution and scalability. *J. Acoust. Soc. Am.* **2012**, *132*, 1780–1791. [[CrossRef](#)]
20. Zhou, Y.; Liang, J.; Maslov, I.K.; Wang, L.H.V. Calibration-free in vivo transverse blood flowmetry based on cross correlation of slow time profiles from photoacoustic microscopy. *Opt. Lett.* **2013**, *38*, 3882–3885. [[CrossRef](#)]
21. Brunker, J.; Beard, P. Acoustic resolution photoacoustic Doppler velocimetry in blood-mimicking fluids. *Sci. Rep.* **2016**, *38*, 3882–3885. [[CrossRef](#)]
22. Kinnunen, M.; Kauppila, A.; Karmenyan, A. Effect of the size and shape of a red blood cell on elastic light scattering properties at the single-cell level. *Biomed. Opt. Express* **2011**, *2*, 1803–1814. [[CrossRef](#)]
23. Fang, H.; Wang, L.H.V. M-mode photoacoustic particle flow imaging. *Opt. Lett.* **2009**, *34*, 671–673. [[CrossRef](#)]
24. Sarimollaoglu, M.; Nedosekin, D.A.; Simanovsky, Y.; Galanzha, E.I.; Zharov, V.P. In vivo photoacoustic time-of-flight velocity measurement of single cells and nanoparticles. *Opt. Lett.* **2011**, *36*, 4086–4088. [[CrossRef](#)]
25. Kiss, B.; Dallinger, S.; Polak K.; Findl, O.; Eichler, H.-G.; Schmetterer, L. Ocular hemodynamics during isometric exercise. *Microvasc. Res.* **2001**, *71*, 1–13. [[CrossRef](#)]
26. Rhinehart, R.R. *Engineering Optimization: Applications, Methods and Analysis*; Wiley: Hoboken, NJ, USA, 2018.
27. Albrecht, H.-E.; Borys, M.; Damaschke, N.; Tropea, C. *Laser Doppler and Phase Doppler Measurement Techniques*; Springer: Berlin/Heidelberg, Germany, 2003.

**Disclaimer/Publisher’s Note:** The statements, opinions and data contained in all publications are solely those of the individual author(s) and contributor(s) and not of MDPI and/or the editor(s). MDPI and/or the editor(s) disclaim responsibility for any injury to people or property resulting from any ideas, methods, instructions or products referred to in the content.